Supporting Information for "Isolated cavities dominate Greenland Ice Sheet ice dynamic response to lake drainages."

J. Z. Mejia[1], J. D. Gulley[1], C. Trunz[2], M. D. Covington[2], T. C. Bartholomaus[3], S. Xie[4], T. Dixon[1]

[1]Department of Geosciences, University of South Florida, 4202 E. Fowler Ave. Tampa, FL 33620.

[2]Department of Geosciences, University of Arkansas, 1 University of Arkansas, Fayetteville, AR 72701

[3]Department of Geological Sciences, University of Idaho, 875 Perimeter Drive, Moscow, ID 83844

[4]Scripps Institution of Oceanography, University of California San Diego, 9500 Gilman Drive, MC 0225, La Jolla, CA 92093

Contents of this file

Introduction

Corresponding author: J. Z. Mejia, Department of Geosciences, University of South Florida, 4202 E. Fowler Dr., Tampa, FL 33620, USA. (jessicamejia@usf.edu)

This supplement provides additional information relating to the main text and details on methodology. **Text S1** elaborates on moulin instrumentation. **Text S2** describes methods used in processing GNSS station data, calculating ice velocities, and determining uplift. **Text S3** elaborates on the procedure used to determine tremor amplitudes and ice quakes from our seismic station SELC. **Text S4** describes the methodology used to determine subglacial routing where **Figure S2** shows the bed topography used in this calculation. **Text S5** and **Figures S6** and **S7** describe our observations during the 2017 lake drainage event at the same location.

Figure S1 shows the satellite imagery constraints on the 2018 lake drainage events. **Figure S3** shows the extended timeseries data over the 2018 melt season, with the addition of surface air temperatures and **Figure S4** shows the relationship between moulin hydraulic head and ice velocity. **Figure S5.** shows the local atmospheric pressure correction. Additionally, **Table S1.** shows locations of our instrumentation and field site while **Table S2.** provides specific information regarding each supraglacial lake drainage.

Text S1.

Moulin instrumentation:

To convert the sensor measurements of water pressure (P_w) to hydraulic head (h) we subtract the piezometer's depth from the GNSS reported ice surface elevation to determine the sensor elevation (z_{sensor}) in meters above sea level. Then, we calculate hydraulic head using the following which assumes a vertical moulin shaft, consistent with uppermost $\sim$ 30 m:

$$h = \frac{P_w}{\rho_w g} + z_{sensor} \tag{1}$$

where ρ_w is the density of water and g is acceleration due to gravity. We estimate an error of 20 m in our absolute moulin head measurements, arising from the uncertainty in the sensor elevation as described in detail in Andrews et al. (2014). Importantly, error in absolute moulin head does not apply to our measurements of relative change (e.g. diurnal variations). We represent moulin hydraulic head as measured from sea-level to allow for comparison with existing datasets and to avoid using poorly constrained bed elevations ($\sim$ 100-meter uncertainty).

We use atmospheric pressures recorded by the GC-NET weather station JAR1 (Steffen et al., 1996), located approximately 5 kilometers northeast of our instrumented moulins JEME (2017) and PIRA (2018). Due to instrument failure, atmospheric pressure variations were not available during the 2018 melt season to correct PIRA hydraulic head. However, the additional error introduced to our 2018 water pressure record is likely small as evidenced by the 2017 correction (Figure S5.) where atmospheric pressure variability is on the order of centimeters (std=0.05 m) while moulin hydraulic head varies on the order of tens of meters (std=34.5 m).

Text S2.

Ice velocity and uplift determination:

Post-processed positions were then imported to Python for further analysis (Virtanen et al., 2020). We transformed into the along-flow and across-flow directions for each station. Before calculating velocities, we filtered positions to reduce spurious signals resulting from GNSS uncertainties by applying a 6-hour rolling mean to each position time series. Velocity is calculated along each component of motion by differencing 2-

hour separated positions. We determined winter background speeds by averaging velocity calculated during periods of continuous measurements between March and May 2018, before the onset of the melt. Formal error is estimated during processing are 1-2 cm in the horizontal direction and 4-5 cm vertically, with a velocity uncertainty of 0.024 m d^{-1}.

Measured vertical ice motion is attributed to a combination of flow along a sloping bed, strain thickening or thinning, and bed separation caused by cavity opening or till dilation where subglacial sediments are present (Howat et al., 2008). To account for changes in elevation associated with bed slope, we detrend the vertical component of motion with respect to distance traveled in the long-flow direction using the linear fit before the melt season when strain and cavity opening should be constant. We transform detrended vertical motion back to the time domain to produce the uplift time series. Consequently, this uplift time series accounts for bed separation due to cavity opening, strain thickening or thinning, and sediment dilation. Previous studies close to our field site (Andrews et al., 2014; Hoffman et al., 2011) have documented significant bed separation over short timescales, suggesting increased bed separation due to cavity growth is likely a significant source of the (> 10 cm) uplift observed during each lake drainage event.

Text S3.

Seismic Analysis:

Glaciohydraulic tremor is characterized by long-duration, low amplitude background seismic noise that varies slowly without clear onset or termination. The amplitude of these ground variations depends on both the flux and the pressure gradient of turbulently-flowing water within efficient, well-connected conduits. We characterized the glaciohy-

draulic tremor amplitude using two different metrics: 1) the median power between 1.5-10 Hz calculated within 1-hr data windows (Bartholomaus et al., 2015), and 2) as the 20th percentile amplitude of enveloped, 10-minute, seismic waveforms, high-pass filtered above 2 Hz. This 20th percentile amplitude was chosen to be well below the higher percentile values that may represent distinct ice fracturing events-equivalent results are obtained for other percentile metrics below approximately 50. Because both measures of glaciohydraulic tremor produced qualitatively similar time series, but the second approach was tailored to work with better temporal resolution, we present the 20th percentile envelope analysis approach.

Distinct from the slowly varying timeseries of glaciohydraulic tremor are distinct, impulsive "icequakes" that typically are found at frequencies greater than 10 Hz. These icequakes are produced by ice fracture events (e.g., crevassing) at the glacier surface, englacially, or at the glacier bed. We quantify the strength of these locally recorded seismic events by the maximum seismic amplitude recorded at our station within 10-minute moving windows. The maximum seismic amplitude depends both on the scale of an event (slip length, stress reduction during the event, and surface area of the fracture surface) and the distance between the event origin and the sensor. Additionally, we examined the seven largest seismic events that occur during the 25 July 2018. These events each consist of paired seismic arrivals on each of three station channels that are consistent with P- and S-waves, very high frequency content ($> 50 - 100$ Hz), inter-phase arrival times that are consistent with a source 500-1000 m from the station (such as the bed), and mostly with downward first P-wave motions, consistent with some kind of crack closing. Some

of these high frequency events had a low-frequency coda consistent with the presence of water. So, while we lack the ability to definitively locate these events, we believe that the high-amplitude icequakes late on 25 July are best explained as ice fracture events at the ice sheet bed.

Text S4.

Subglacial routing via hydraulic potential gradients.:

Subglacial routing via hydraulic potential gradients. We estimate subglacial hydraulic potential gradients (ϕ) following:

$$\phi = \rho_w g z_b + P_w \tag{2}$$

where ϕ_w is the density of water, g is acceleration due to gravity, z_b is bed elevation, and P_w is subglacial water pressure, assumed to be equal to ice overburden pressure (or $\rho g h$, where ρ_i is ice density and h is the ice thickness). Surface and bed elevations (Figure S2) are derived from the BedMachine Greenland v3 dataset (Morlighem et al., 2017) with a 150 m-resolution (true resolution 400 m). This calculation requires the assumption that subglacial water pressures are at overburden throughout the domain during conduit formation. Once conduit flow paths are established, they can expand by melting and contract by creep closure but their locations are unlikely to change (Gulley et al., 2012). We determine flow paths by calculating flow accumulation along subglacial hydropotential gradients using the MATLAB topotools toolbox (Schwanghart & Kuhn, 2010). We use surface and bed elevations at points spaced 50-m along the hydropotential flow path connecting Lake E to the terminus (bold pink line) for the bed profile in Figure 1c.

While our observations show a direct connection between a draining supraglacial lake and a moulin located over eight kilometers downglacier, instrument records suggest the floodwave modified an even larger area of the subglacial drainage system. The similarity between the GNSS station response to each lake drainage event indicates the lateral extent of the floodwave was at least 500 m, which is approximately equivalent to the ice thickness in this area. We argue that our observations reflect the lower limit on the area of the isolated drainage system dewatered by the subglacial floodwave. It is likely that similar alterations to the subglacial drainage system occurred at downglacier locations as the floodwave continued propagating towards the coast.

Text S5.

Isolated cavities dominate Greenland Ice sheet dynamic response to lake drainage:

On 21 July 2017, we instrumented JEME moulin with a pressure transducer that was anchored 350 m below the ice surface. By July 2018, moulin JEME had been advected 90 m downglacier, consistent with measured annual ice displacement of approximately 90 m a^{-1}. On 10 July 2018, we instrumented the new moulin, PIRA, which opened in the same position on the ice sheet as JEME the year before. In 2017, Sentinel-2A and Landsat 8 imagery captured three supraglacial lake drainages between 26-27 July (**Figure S6**; Lakes A and B; **Figure S7**). On 27 July at 02:30UTC, moulin water levels deviated from their nightly decline as the subglacial floodwave created by the lake drainages approached our site. By 04:30 UTC, moulin water level had jumped more than 60 m (about 13

Over the week following the lake drainage event minimum moulin water levels declined. By 3 August, the diurnal minimum moulin water level was 60 m lower than after the lake drainage event when ice velocities initially fell to wintertime background speeds. Despite this significant reduction in minimum moulin water level (for comparison, during the lake drainage event moulin water levels increased by 60 m) minimum ice velocity remained at winter background speeds, unaffected by the falling pressures within the active drainage system. This observation contradicts the behavior expected if increased efficiency of the channelized drainage system slowed sliding speeds. Therefore, while increased pressurization of the active drainage system reduced basal traction to drive diurnal acceleration, declining pressures in the active drainage did not reduce minimum sliding speeds. Instead, these observations indicate the state of the isolated drainage system governed the lower limit of sliding speeds.

References

Andrews, L. C., Catania, G. A., Hoffman, M. J., Gulley, J. D., Lüthi, M. P., Ryser, C., ... Neumann, T. A. (2014). Direct observations of evolving subglacial drainage beneath the Greenland Ice Sheet. *Nature*, *514*(7520), 80–83. Retrieved from `http://www.nature.com/doifinder/10.1038/nature13796` doi: 10.1038/nature13796

Bartholomaus, T. C., Larsen, C. F., Amundson, J. M., O'Neel, S., Walter, J. I., & West, M. E. (2015). Subglacial discharge at tidewater glaciers revealed by seismic tremor. *Geophysical Research Letters*, *42*, 6391–6398. doi: 10.1002/2015GL064590.Received

Gulley, J. D., Grabiec, M., Martin, J. B., Jania, J., Catania, G. A., & Glowacki, P. S. (2012). The effect of discrete recharge by moulins and heterogeneity in flow-path

efficiency at glacier beds on subglacial hydrology. *Journal of Glaciology*, *58*(211), 926–940. doi: 10.3189/2012JoG11J189

Hoffman, M. J., Catania, G. A., Neumann, T. A., Andrews, L. C., & Rumrill, J. A. (2011). Links between acceleration, melting, and supraglacial lake drainage of the western Greenland Ice Sheet. *Journal of Geophysical Research: Earth Surface*, *116*(4), 1–16. doi: 10.1029/2010JF001934

Howat, I. M., Tulaczyk, S. M., Waddlngton, E. D., & Björnsson, H. (2008). Dynamic controls on glacier basal motion inferred from surface ice motion. *Journal of Geophysical Research*, *113*(F3), F03015. Retrieved from `http://doi.wiley.com/10.1029/2007JF000925` doi: 10.1029/2007JF000925

Morlighem, M., Williams, C. N., Rignot, E., An, L., Arndt, J. E., Bamber, J. L., ... Zinglersen, K. B. (2017). BedMachine v3: Complete Bed Topography and Ocean Bathymetry Mapping of Greenland From Multibeam Echo Sounding Combined With Mass Conservation. *Geophysical Research Letters*, *44*(21), 051–11. doi: 10.1002/2017GL074954

Morriss, B. F., Hawley, R. L., Chipman, J. W., Andrews, L. C., Catania, G. A., Hoffman, M. J., ... Neumann, T. A. (2013). A ten-year record of supraglacial lake evolution and rapid drainage in West Greenland using an automated processing algorithm for multispectral imagery. *Cryosphere*, *7*(6), 1869–1877. doi: 10.5194/tc-7-1869-2013

Schwanghart, W., & Kuhn, N. J. (2010). TopoToolbox: A set of Matlab functions for topographic analysis. *Environmental Modelling and Software*. doi: 10.1016/j.envsoft.2009.12.002

Steffen, C., Box, J. E., & Abdalati, W. (1996). Greenland Climate Network: GC-Net. *Cold Regions Research and Engineering Laboratory*, *CRREL Spec*, 98–103.

Virtanen, P., Gommers, R., Oliphant, T. E., Haberland, M., Reddy, T., Cournapeau, D., ... Vázquez-Baeza, Y. (2020). SciPy 1.0: fundamental algorithms for scientific computing in Python. *Nature Methods*, *17*, 261–272. doi: 10.1038/s41592-019-0686-2

Williamson, A. G., Arnold, N. S., Banwell, A. F., & Willis, I. C. (2017). A Fully Automated Supraglacial lake area and volume Tracking ("FAST") algorithm: Development and application using MODIS imagery of West Greenland. *Remote Sensing of Environment*, *196*, 113–133. Retrieved from `https://doi.org/10.1016/j.rse.2017.04.032` doi: 10.1016/j.rse.2017.04.032

Table S1. Field instrumentation locations

	Latitude °N	Longitude °E	Elevation (m)	Ice thickness (m)	
JEME & PIRA moulins	69.4741	-49.8232	779	503	supraglacial stream entering from east
JEME GNSS 2018	69.4738	-49.8249	797	503	$\sim$ 90 m southwest (downglacier) from PIRA moulin
LMID GNSS	69.4708	-49.8189	796	514	uncrevassed, local high
JNIH GNSS	69.4684	-49.8318	790	547	uncrevassed, near small supraglacial stream and moulin
LC weather station	69.4727	-49.8263	777	512	uncrevassed, supraglacial streams to north and south
LC seismic station	69.4734	-49.8208	781	498	only active during 2018.

Lake	Max Area (km^2)	Volume** (m^3)	Latitude °N	Longitude °E	Elevation (m.a.s.l.)	Ice thickness (m)	Distance (km) Direct	Subglacial
A 63*	(0.633) 0.946	(4.9)8.6$\times10^5$	69.4537	-49.6247	888	728	7.4	8.9
B 59	(0.331) 0.362	(2.4)2.6$\times10^5$	69.4710	-49.6272	930	673	7.4	9.8
C 68	1.963	2.8$\times10^6$	69.4355	-49.5297	913	882	12.3	13.4
D 57	0.490	3.6$\times10^5$	69.4764	-49.3836	1021	918	17.4	22.2
E 50	1.365	1.5$\times10^6$	69.4897	-49.2151	1100	1065	23.8	33.3
F 43	1.350	1.5$\times10^6$	69.5343	-49.1291	1131	1120	27.9	40.2
G 45	0.493	3.6$\times10^5$	69.5253	-49.1952	1159	1020	25.2	37.6
H 38	0.701	5.6$\times10^5$	69.5496	-49.1801	1159	1100	26.5	40.6
I 35	2.300	3.8$\times10^6$	69.5724	-49.2104	1146	1020	21.5	33.7
J 33	1.224	1.3$\times10^6$	69.5680	-49.3410	1115	1160	26.4	37.6

* numbers correspond with Morriss et al. (2013) naming conventions

** values have an associated error of 0.420×10^6 m^3.

() denote values associated with 2017 lake drainage events.

Table S2. Volume estimated using an area-to-volume scaling relationship for the Paakitsoq region (Williamson et al., 2017).

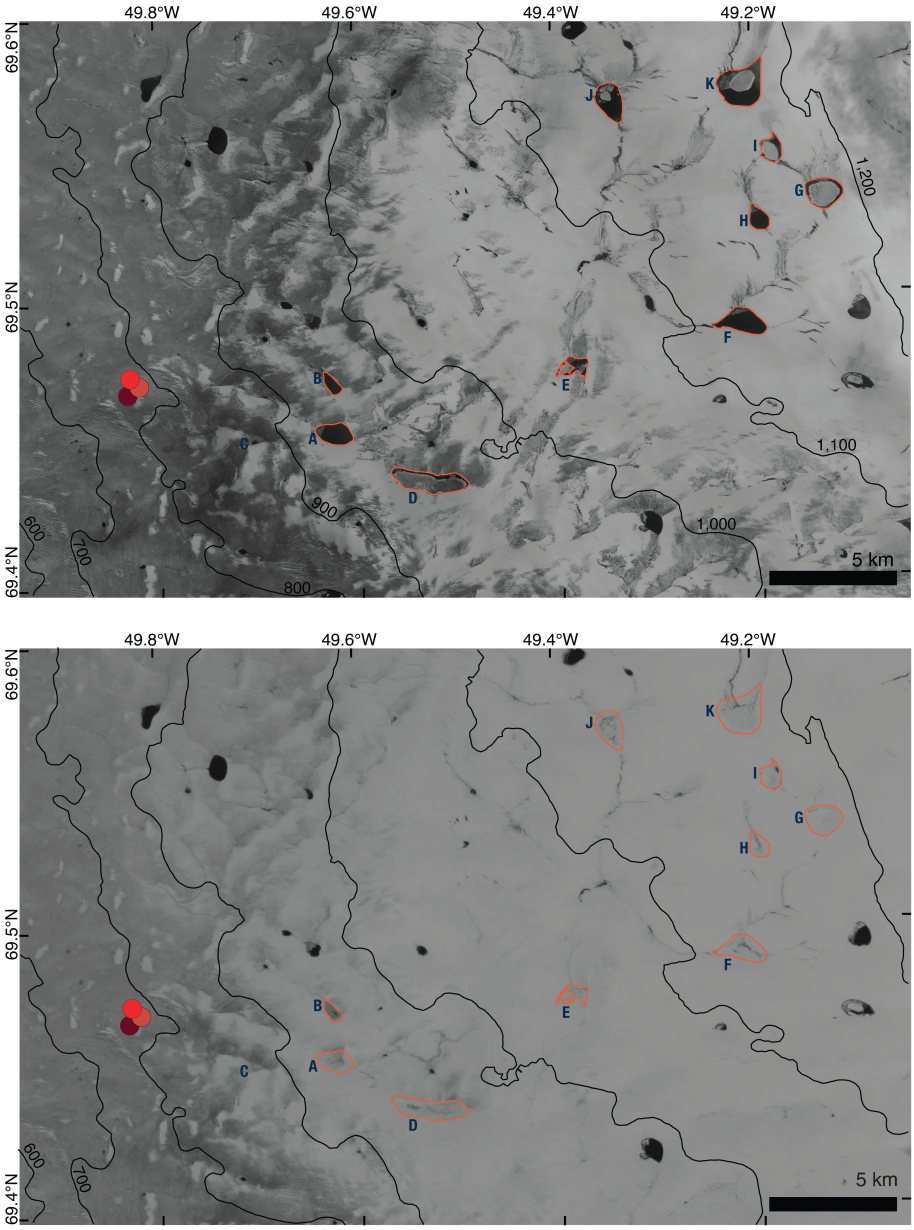

Figure S1. Satellite imagery constrains on 2018 lake drainage. (a) Copernicus Sentinel image acquired on 24 July 2018 at 15:29:11 UTC showing the maximum extents of supraglacial lakes A-J (red outlines), with the location of our instruments (red circles). (b) Landsat-8 image acquired on 30 July 2018 at 14:59:53 UTC showing the drainage of lakes A-J, maximum extents same as in a. Surface elevation contours (m) are from BedMachine-v3. Data available from the U.S. Geological Survey

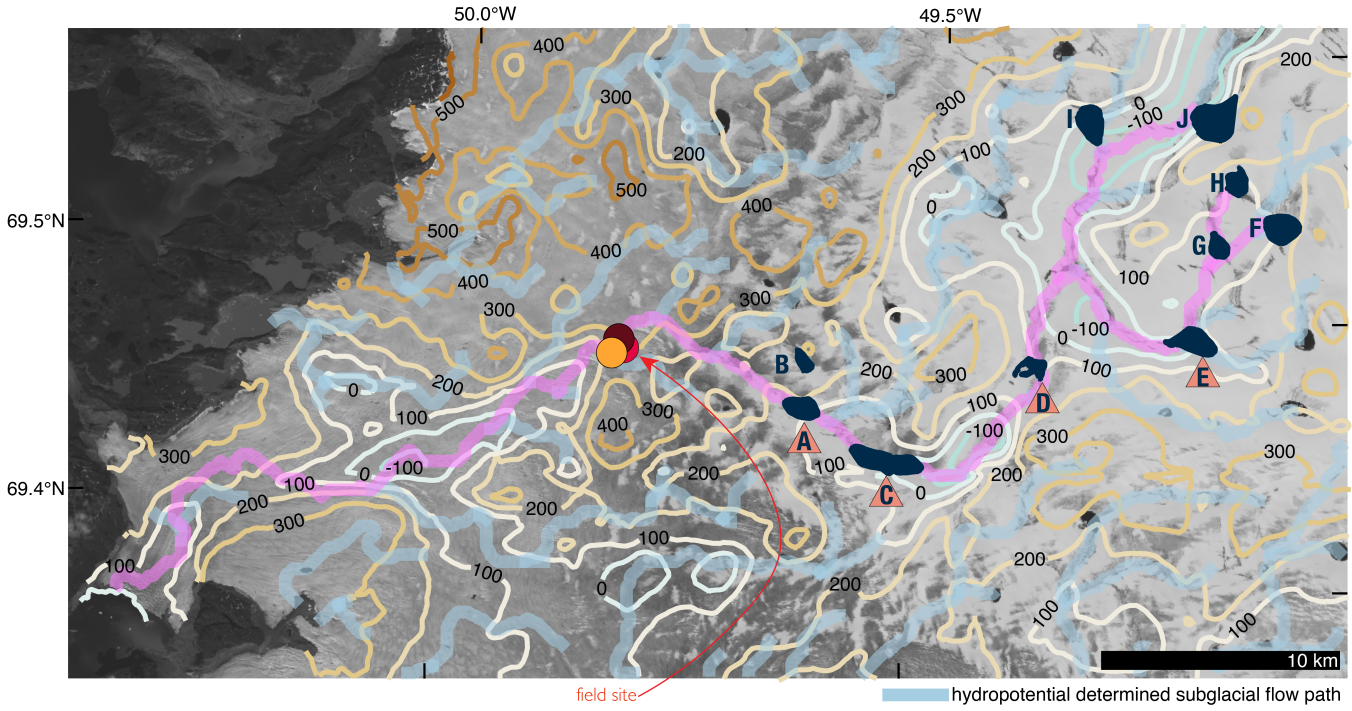

Figure S2. Bed topography and hydropotential predicted subglacial flow routing. BedMachine derived bed elevation contours are shown in meters. Subglacial flow routing from hydropotential gradients is shown in light blue. Supraglacial lakes mentioned in the main text are labeled and their maximum extents are marked in navy.

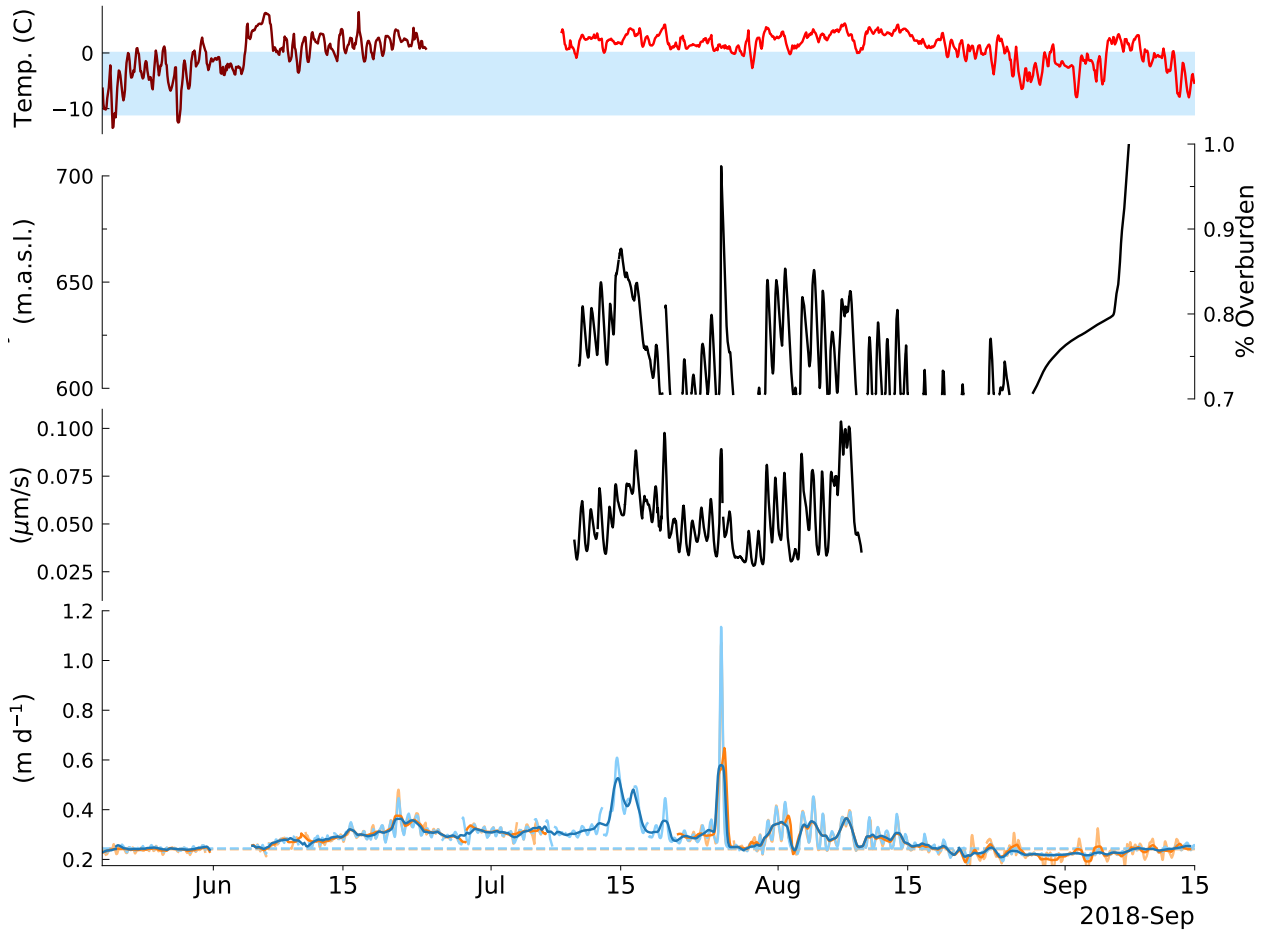

Figure S3. (a) Surface air temperature recorded at LOWC weather station (red) and the GC-NET station JAR1 (maroon). (b) Moulin hydraulic head in m.a.s.l. and fraction of overburden for an ice thickness of 503 m. (c) Glaciohydraulic tremor amplitude smoothed with a 6-h rolling mean. (d) Along-flow ice velocity measured at stations JEME (orange) and LMID (blue). Light colors are smoothed with a 6-h rolling mean to show diurnal variability and light colors are smoothed with a 24-hr rolling mean emphasize the slowdown following the mid-season lake drainage event. Blue and orange dashed lines mark winter background sliding speeds.

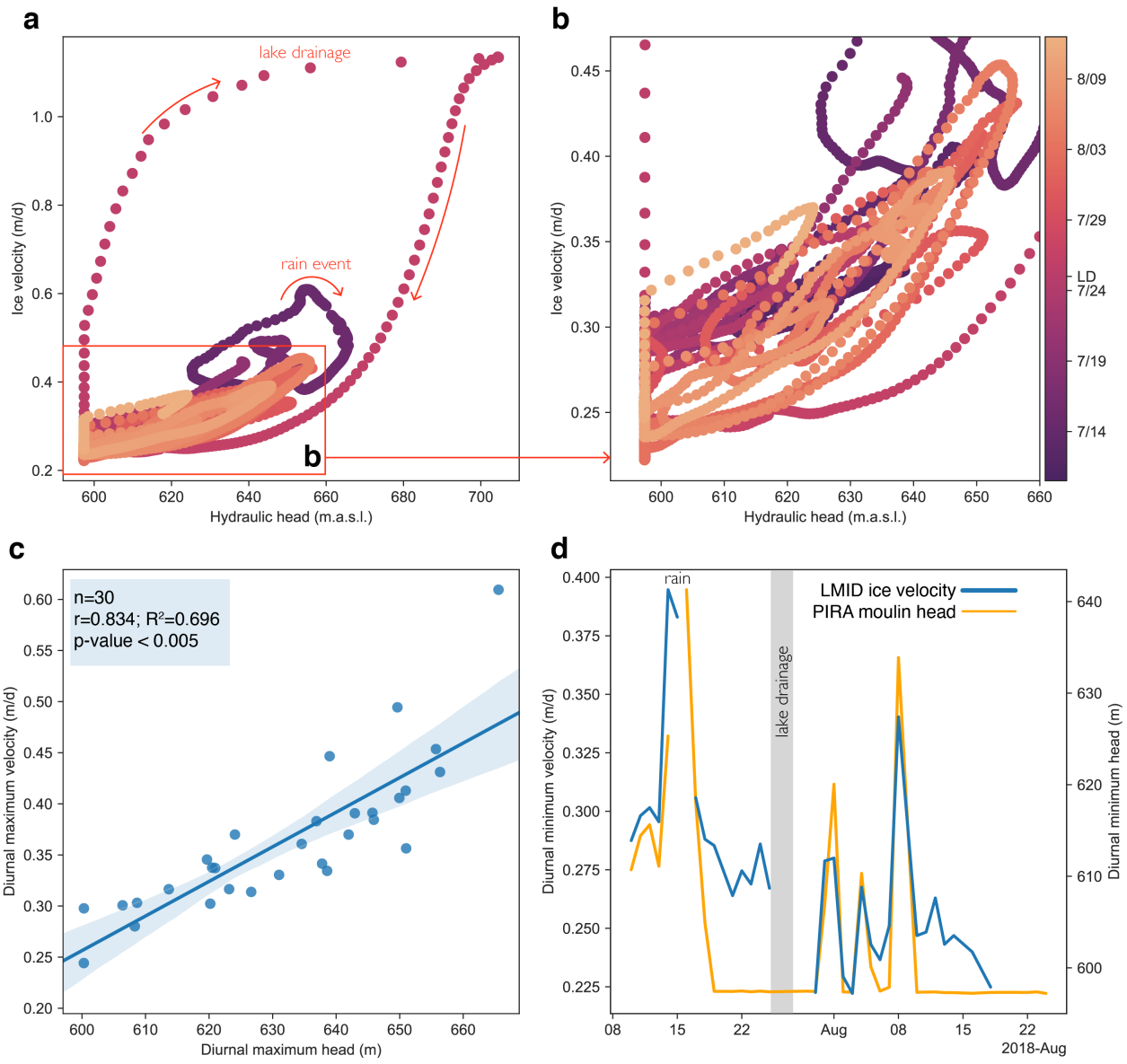

Figure S4. (a-b) Moulin hydraulic head and ice velocity variations coloring reflects the date of the measurements. A zoom in to diurnal variations is shown in b. Diurnal variations move in a clock-wise pattern. (c) Linear regression between diurnal maximum moulin hydraulic head and ice velocity ($n = 30, r = 0.834, p < 0.05$). (d) Diurnal minimum ice velocity and moulin head plotted though time.

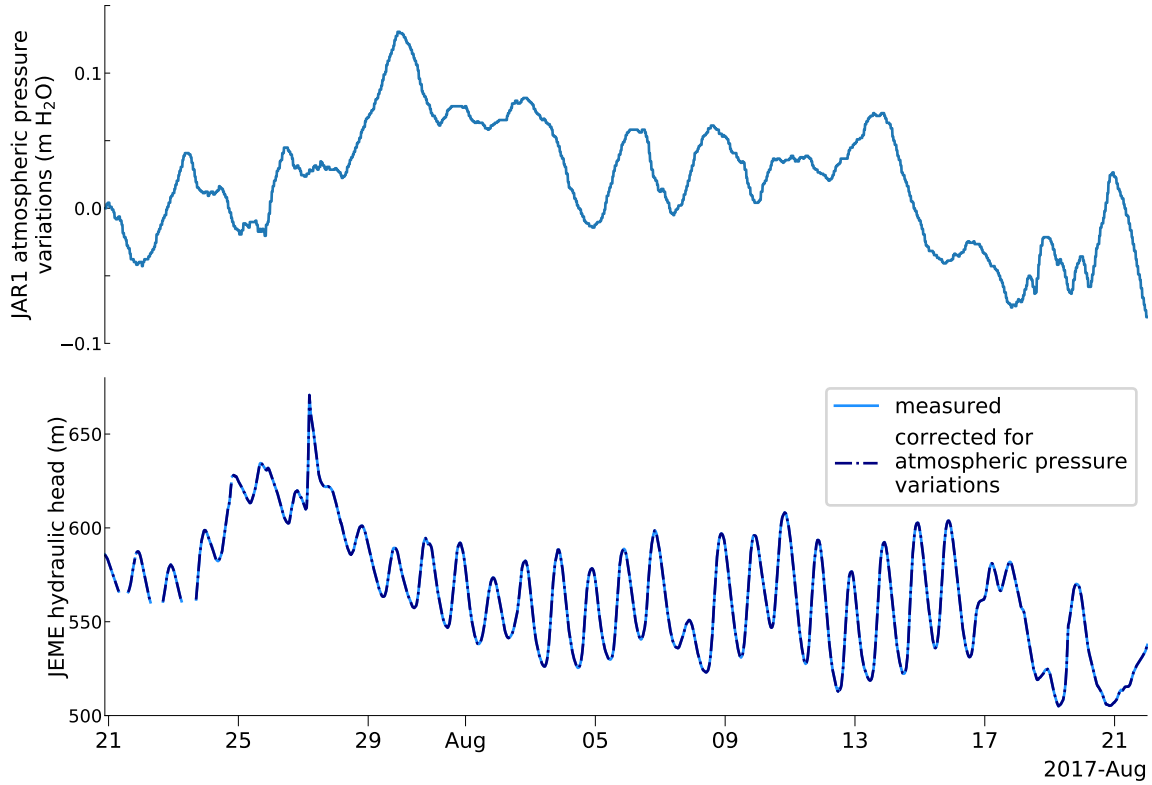

Figure S5. 2017 Atmospheric pressure variability. (a) Atmospheric pressure measured at JAR1 less the atmospheric pressure at the time JEME moulin was instrumented (9.2422 m H2O). (b) Hydraulic head measured at JEME moulin (blue), and moulin head corrected for atmospheric pressure variability shown in a, (navy dashed line).

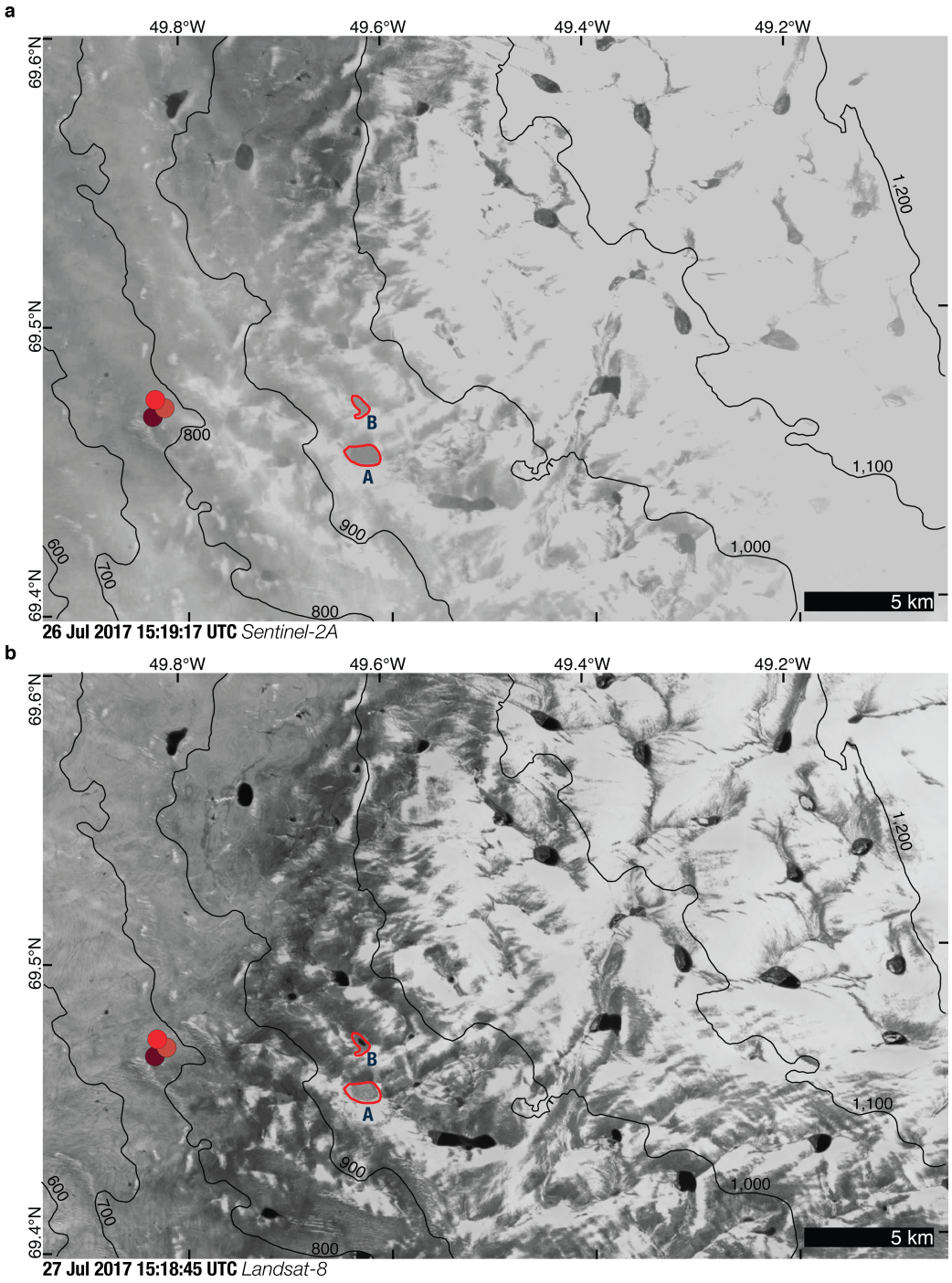

Figure S6. Satellite imagery constraints on 2017 lake drainages. a, Sentinel-2A image from 26 July 2017 at 15:18:17 UTC showing the maximum extents of supraglacial lakes A and B (red), with the location of our instruments (red circles). b, Landsat-8 image acquired on 27 July 2017 at 15:18:45 UTC showing the drainage of lakes A and B, maximum extents same as in a. Surface elevation contours (m) are from BedMachine-v3.

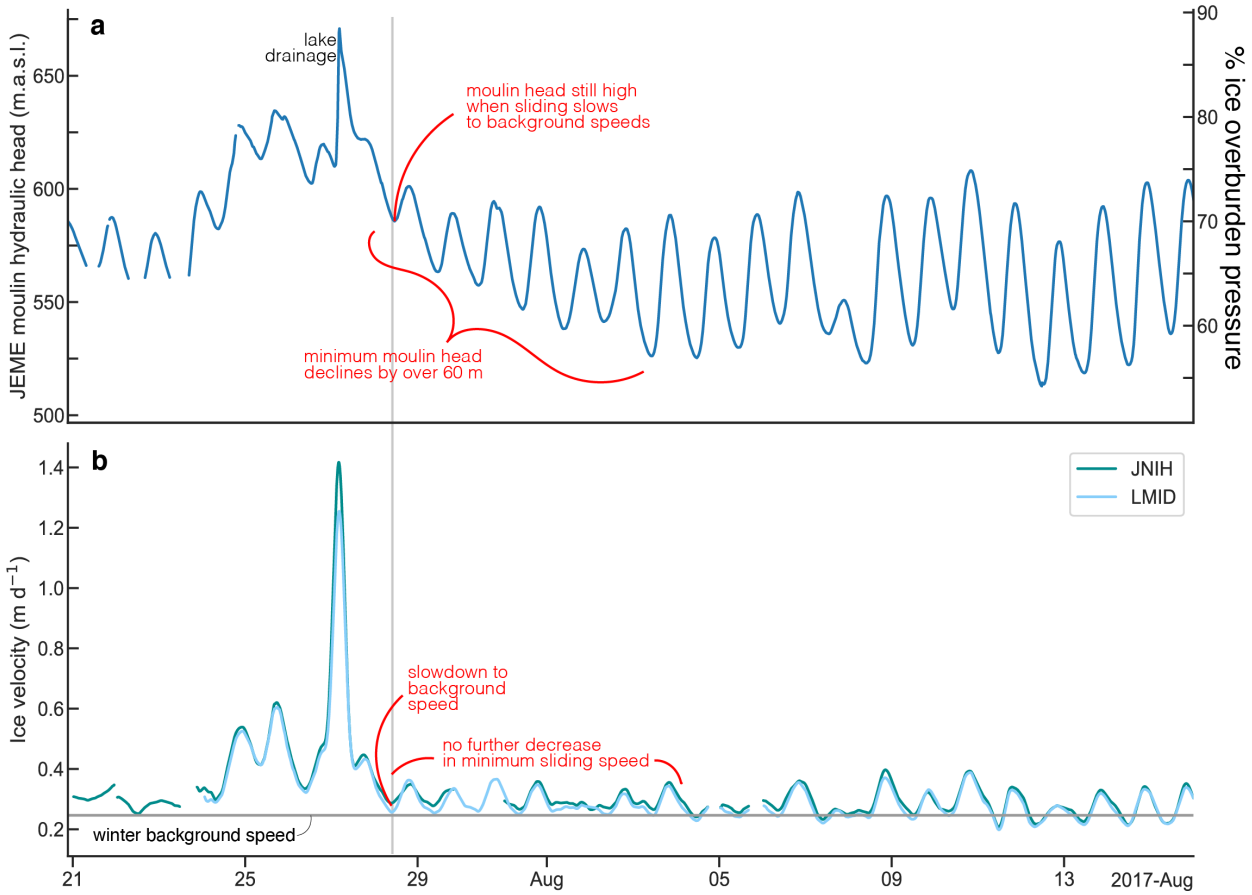

Figure S7. Moulin head and ice velocity timeseries showing 2017 lake drainage event. a, JEME moulin hydraulic head (located in the same position as PIRA which formed in its place during early 2018). b, Along-flow ice velocity from stations LMID (light blue) and JNIH (teal). This timeseries is interrupted by the passing of subglacial floodwaters on 28 July 2017. Sliding slows to winter background speeds (gray) despite high moulin head. Diurnal minimum moulin head falls over the subsequent week, amounting to 60 m (same magnitude as the lake drainage increase) but there is no further decrease in ice velocity as would be expected if increased channelization controlled minimum sliding speed.